Proceedings of the Canadian Society for Mechanical Engineering International Congress
32nd Annual Conference of the Computational Fluid Dynamics Society of Canada
Canadian Society of Rheology Symposium
CSME/CFDSC/CSR 2025
May 25–28, 2025, Montréal, Québec, Canada

Development of a Low Cost Characterization Method for Drone-scale Aircraft Electric Motors

Pascal Bérubé[1], Charles Blouin[2], Baiyun Tang[2], David Rancourt[1],

[1]Createk Innovation Group, Interdisciplinary Institute for Technological Innovation, Université de Sherbrooke, Sherbrooke, Canada
[2]Tyto Robotics Inc., Gatineau, Canada

***Abstract*—**This paper presents a low-cost characterization method to quickly assess the efficiency of brushless DC (BLDC) motors and ESC (Electronic Speed Control) combos across their entire torque-speed range. A belt-driven dynamometer, developed to fit on a commercially available flight stand with off-the-shelf parts, is used to characterize motors under real-world conditions. The setup minimizes vibrations and allows each motor to spin on its own axis, providing comprehensive motor efficiency maps. The results demonstrate the effectiveness of the testbed in offering quick and accurate characterization, highlighting the impact of ESC on motor efficiency. This approach provides valuable insight into operational characteristics and can be used for academic purposes to teach students about component selection and usage. Access to efficiency maps for drone-sized motors opens the door to improved powertrain design and longer flight times.

***Keywords-component*—BLDC motor, characterization method, belt-driven dynamometer, testbed, motor performance, efficiency map.**

I. Introduction

In recent years, there has been growing interest in Unmanned Aircraft Vehicles (UAVs) as they become more affordable and performant. From structure inspection to goods delivery, they are used to simplify otherwise complex or trivial tasks [1]. One challenging step in the design process for drone-scale aircraft (both fixed-wing and multicopter) is the powertrain design or selection. In addition to batteries, electronic speed control (ESC), motor, and propeller must be modeled throughout the entire operating range. While creating propeller performance models is relatively straightforward, creating accurate motor and ESC models is considerably more challenging. Motor and ESC manufacturers typically do not provide comprehensive data for their products except for limited peak values for power and current, and occasionally thrust values in static conditions or efficiencies when coupled with a propeller. Essentially, drone designers must experimentally characterize each motor and ESC. Then, by adding the propeller performance model, one can numerically simulate the powertrain performance in all flight conditions, thus selecting more appropriate components that lead to better-performing aircraft.

Motor characterization is a well-documented process in which dynamometers are used to map the efficiency of motors of all sizes across the whole range of speed and torque. Commercially available solutions typically fall into three categories. First, there are inertial wheels from which one can derive the torque based on the speed and inertia of the wheel. Although relatively inexpensive, the large flywheel is subject to aerodynamic drag as a result of air resistance and assumes no time dependence on the performance of the components. The second possibility is to use a mechanical brake (Prony brake) to counteract the torque of the motor [2]. This method, while also low-cost, produces a significant amount of heat from the braking friction. Furthermore, constant slippage between components results in accelerated degradation. Lastly, a generator can be used as an electrical brake. The generated power can be dropped into a resistive load [3] or returned to the DC bus to reduce the load on the power supply [4], [5]. Unfortunately, most of the proposed setups use a face-to-face assembly. Although this configuration allows for a compact design, it is usually custom-made for a specific motor, and thus lacks adaptability. Furthermore, this architecture is prone to vibrations due to balancing and alignment challenges, limiting their applications to low-speed/high-torque motors.

To address these limitations, this paper presents a validated low-cost experimental setup for characterizing BLDC motors. To keep the cost to a minimum, the dynamometer is developed to fit on a commercially available flight stand with off-the-shelf parts. The method and testbed are demonstrated on

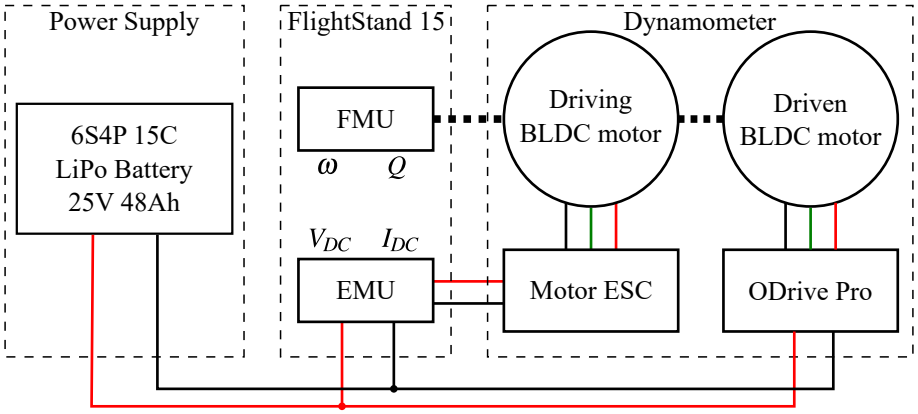

Figure 1. Schematic representation of the testbed and its components

the Cobra 4130/12 (Danlions Electric Industrial Co., Ltd.) and Cobra 4130/20 (Danlions Electric Industrial Co., Ltd.) motors typically used on airplanes. In order to produce a full motor efficiency map, both mechanical and electrical power are monitored. Mechanical power is sampled directly on the motor body, while electrical power is sampled on the DC side of the motor ESC. As stand-alone ESC characterization is a cumbersome process [6] and of low interest in this study, the motor and ESC are characterized as a whole. To avoid the rotordynamic issues mentioned earlier, a belt-driven setup is used to allow each motor to spin on its own axis.

The findings of this study aim to advance powertrain design by providing a solution to model the motor and the ESC throughout their operating ranges. This work serves as a first step in modeling complete powertrains, including batteries and propellers, which will lead to more capable, energy-efficient, and cost-effective drones.

II. Methodology

A. Dynamometer architecture

Fig. 1 illustrates a schematic representation of the testbed. The electrical power travels from the power supply through the Electrical Measurement Unit to the ESC. The EMU monitors the voltage V_{DC} as well as the current I_{DC}. The speed (ω) and torque (Q) of the motor are measured directly using a Flight Stand 15 (Tyto Robotics Inc.) through the Force Measurement Unit (FMU), which is equipped with a load cell and an optical sensor. Mechanical power is then transferred to the generator through a belt and finally returned to the DC bus to help reduce the load on the power supply. The belt configuration offers many advantages over the traditional face-to-face design. First, since both motors are spinning on their own axes, there is little to no vibration even at higher speeds. In addition, the belt has a damping effect on the testbed. Secondly, the pulley ratio can be modified to accommodate an even larger spectrum of motors without the need for a new generator. The dynamometer uses bearing supports with a rigid link between the motors to compensate for the induced bending created by the belt side load. Finally, a static belt tensioner provides a constant belt tension throughout the characterization. A visual representation of the current configuration of the testbed is provided in Fig. 2. This testbed was designed to characterize the efficiency of any small- to medium-size BLDC and its ESC combo.

The motor used on the driven side is the same as the driver side for design simplicity, but any motor with equivalent or greater power output that fits within the testbed constraints could be used. Adjustments in the pulley ratio may be necessary to accommodate variations in motor specifications. The drive for this motor is an ODrive Pro (ODrive Robotics Inc.) that operates in the range $12\,\mathrm{V}$ to $56\,\mathrm{V}$. It can support a continuous current of $80\,\mathrm{A}$ with peak current at $120\,\mathrm{A}$ for $3\,\mathrm{s}$ if it is fitted with a proper heat sink and fan. This drive can control the motor in either position, velocity, or torque if paired with an encoder. To this end, an AMT102 encoder (Same sky) set to 512 pulses per revolution allows motor control up to $15{,}000\,\mathrm{rpm}$. The ODrive is controlled with a Python script through an API provided by the manufacturer.

The power supply consists of four Graphene Professional $12{,}000\,\mathrm{mA\,h}$ 6S 15C LiPo batteries (Turnigy) connected in parallel, providing more than 30 minutes of continuous testing capability for the selected motor. The four batteries deliver $25\,\mathrm{V}$ at full charge and $48\,\mathrm{A\,h}$ at 1C.

The whole dynamometer is designed to fit on Tyto Robotic's Flight Stand 15. The FMU is equipped with a load cell that reads the torque (Q) between $\pm 8\,\mathrm{N\,m}$ with a resolution of $0.001\,\mathrm{N\,m}$ at a sampling rate of $1000\,\mathrm{Hz}$. The precision is $\pm 0.75\,\%$ of the measured value. The FMU also has an optical speed sensor that reads rpm (ω) from $0\,\mathrm{rpm}$ to $30{,}000\,\mathrm{rpm}$ with a precision of $\pm 1\,\mathrm{rpm}$.

The Flight Stand is also equipped with an Electrical Measurement Unit (EMU) that monitors both the voltage (V_{DC}) and the current (I_{DC}) of the motor at a sampling rate of $1000\,\mathrm{Hz}$. The voltage sensor has a range of $0\,\mathrm{V}$ to $180\,\mathrm{V}$ with a resolution of $0.001\,\mathrm{V}$ and a precision of $1\,\%$ of the measured value. The Hall effect current sensor ranges from $0\,\mathrm{A}$ to $150\,\mathrm{A}$ with a resolution of $0.001\,\mathrm{A}$ and a precision of $1\,\%$ of the measured value.

Finally, since this type of motor is designed to be cooled by the propeller air stream, the overheating of the motors and

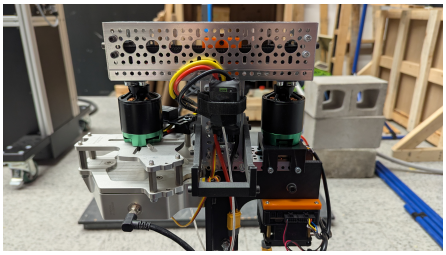

(a) General view without cooling

(b) General view with cooling

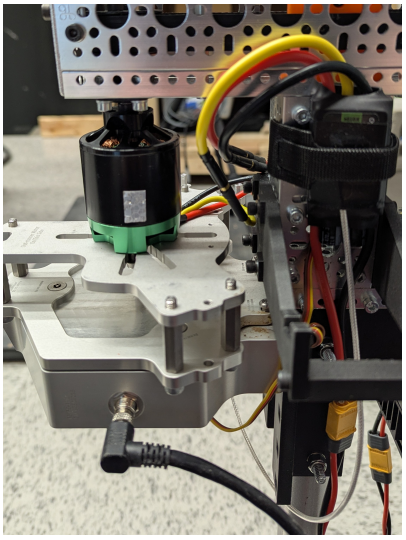

(c) Driving side: shows the characterized motor, ESC, and FMU

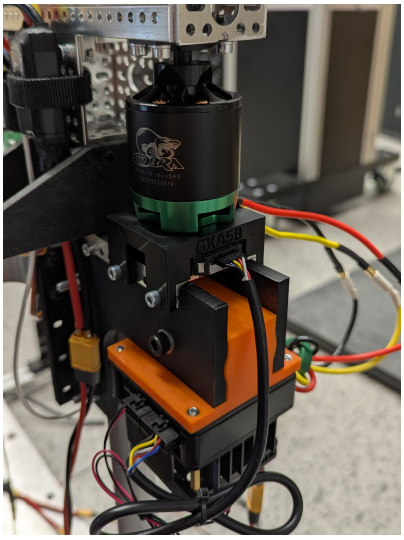

(d) Driven side: shows the driven motor, the Odrive, and the AMT102 encoder

Figure 2. Views of the dynamometer designed for this study

the ESC is mitigated by employing three $120\,\mathrm{mm} \times 120\,\mathrm{mm}$ cooling fans.

B. Control Strategy and Experimental Procedure

The experimental process can be summarized as follows. First, the motor ESC is activated to reach a target no-load rpm with no load on the generator. Once the target point is achieved, the system acquires data for $3\,\mathrm{s}$, allowing motor stabilization. Then, the ODrive activates and maintains the selected speed. Next, the PWM of the motor increases in steps of $1\,\mu\mathrm{s}$ until the motor current reaches the target or exceeds the threshold ΔI_{DC}. Another stabilization period of $3\,\mathrm{s}$ is introduced. This PWM increment process continues until the current exceeds limits or speed slippage occurs. From this point on, the ODrive stops and the motor is free to spin. This process is repeated until the entire range of speeds is covered.

However, the relationships of PWM to speed and PWM to current are nonlinear, as can be observed in Fig. 3. Equally spaced steps of $5\,\mu\mathrm{s}$ result in a poorly distributed grid, with samples concentrated mainly in the low-current part of the map. Although there are control solutions for nonlinear systems [7], [8], implementing them can be complex. Even simple PID controllers may need adjustments for each new motor to be mapped.

Instead of incremental steps to reach the desired speed, a no-load run of the motor is performed to produce a map of the relation between PWM and speed. The speed steps $\Delta\omega$ are determined with

$$\Delta\omega = \frac{\omega_{max} - \omega_{min}}{n} \tag{1}$$

where ω_{min} is the minimal stable speed value at which the motor spins without stalling due to friction. ω_{max} is the maximum speed during the zero-load run. Lastly, n is the number of discretizations tested, which is set to 10 for this study. Once the motor stabilizes at a new speed, the ODrive Pro maintains this speed using the encoder to evaluate the speed. Beyond this point, further increases in PWM lead to an increase in current (torque) rather than speed.

The proposed method to control the current, although not linear, is designed for a gradual increase in current. PWM is raised in $1\,\mu\mathrm{s}$ steps every $0.1\,\mathrm{s}$. Doing so ensures that the current I_{DC} increases by at least ΔI_{DC}, which is defined as

$$\Delta I_{DC} = \frac{I_{DC_{max}} - I_{DC_{start}}}{n} \tag{2}$$

where $I_{DC_{start}}$ is the current at the moment the control switches to the current control. The interval ΔI_{DC} is redefined for every new speed. Sampling for specific values of current over $3\,\mathrm{s}$ instead of a continuous sweep allows averaging the values and reducing noise. This approach helps smooth out the results later when interpolating over the data. Although this approach sacrifices some grid uniformity, it provides a low-cost alternative to implementing complex controller logic. As seen in Fig. 4, this approach still fills the grid relatively uniformly.

In both Fig. 3 and 4, the upper left corner of the sampling space remains unpopulated. As the torque increases, the ODrive struggles to maintain the speed of the generator and eventually starts to slip. As this section of the map is of low interest for aircraft powertrain applications, if the controller detects $\delta\omega \geq 100\,\mathrm{rpm}$ variation in the target speed, the sequence stops, progressing to the next speed value. This phenomenon can be observed in Fig. 3, where some of the points are slightly shifted compared to the rest of the column.

C. Data post-processing

At every point in the sampling space, the EMU determines the electrical power P_e supplied to the DC side of the driving

motor ESC

$$P_e = V_{DC} I_{DC} \tag{3}$$

where V_{DC} is the measured voltage in volts V in and I_{DC} is the measured current in amps A drawn from the power supply. The FMU determines the mechanical power output by the motor

$$P_m = Q\omega \tag{4}$$

where Q is the measured torque in N m and ω is the measured rotational speed in $\mathrm{rad\,s^{-1}}$. From (3) and (4), it is now possible to determine the overall efficiency of the motor and the ESC with (5).

$$\eta = \frac{P_m}{P_e} = \frac{Q\omega}{VI} \tag{5}$$

To determine the uncertainty in the efficiency η, we use the propagation of uncertainties as defined in

$$u_f = \sqrt{\left(\frac{\partial f}{\partial x} u_x\right)^2 + \left(\frac{\partial f}{\partial y} u_y\right)^2 + \left(\frac{\partial f}{\partial z} u_z\right)^2 + \dots} \tag{6}$$

Using the definition of (5) in (6) and assuming that the error in speed is negligible, we obtain the following

$$u_\eta = \sqrt{\left(\frac{Q \cdot \omega}{V^2 \cdot I} u_V\right)^2 + \left(\frac{Q \cdot \omega}{V \cdot I^2} u_I\right)^2 + \left(\frac{\omega}{V \cdot I} u_Q\right)^2} \tag{7}$$

which can be simplified to

$$\frac{u_\eta}{\eta} = \sqrt{\left(\frac{u_V}{V}\right)^2 + \left(\frac{u_I}{I}\right)^2 + \left(\frac{u_Q}{Q}\right)^2} \tag{8}$$

where $\frac{u_X}{X}$ is the relative error of the variable. Given the relative uncertainties $\frac{u_V}{V} = 0.01$, $\frac{u_I}{I} = 0.01$ and $\frac{u_Q}{Q} = 0.0075$, the uncertainty $\frac{u_\eta}{\eta}$ is calculated as:

$$\frac{u_\eta}{\eta} = \eta\sqrt{(0.01)^2 + (0.01)^2 + (0.0075)^2} \approx 0.016 \tag{9}$$

Therefore, the uncertainty in the efficiency η is approximately $\pm 1.6\,\%$.

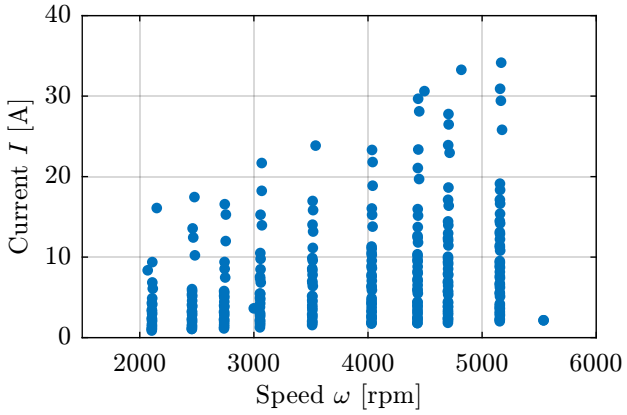

Figure 3. Constant PWM increments of 5 µs

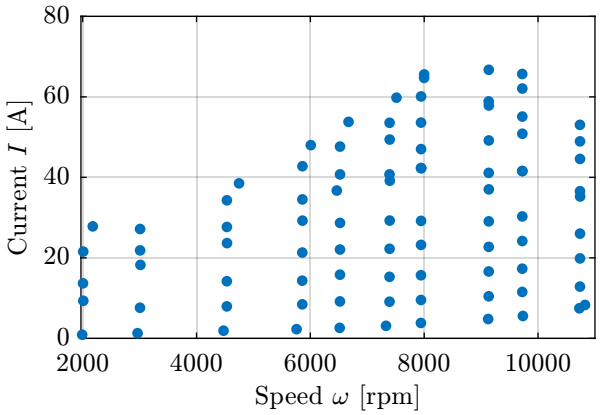

Figure 4. Speed and current control using the proposed logic

TABLE I: Statistical data of speed centring

Means	Max	Min	Std Dev
2039	2177	1991	77.9
3001	3015	2964	20.6
4556	4747	4474	87.2
5865	6007	5758	67.5
6531	6671	6465	55.7
7398	7513	7329	45.0
7954	8000	7942	21.3
9133	9136	9124	3.4
9725	9734	9722	3.3

The complete set of data acquired from the test sequence cannot be used as is to generate an efficiency map. Since sampling is performed continuously at 1000 Hz, either curve fitting is required or interpolation on averaged data may be used. In this work, the second approach is taken. Fig. 4 presents the agglomeration of samples for each characterized usage case. Each dot is the average of each 3 s sampled. Since the generator is controlled in RPM, most "vertical rows" from Fig. 4 can essentially be considered at fixed RPM. By forcing the values to be constant, the interpolation schemes are more robust and smooth. Table I presents the variation in RPM for every group of speeds; the standard deviation is negligible, and so is the effect of this smoothing process.

III. Results and Discussion

In this paper, two motors were characterized to demonstrate the capability of the testbed: the Cobra 4130/12 KV540 and the Cobra 4130/20 KV300. The technical specifications for these motors can be found in table II. Both motors are controlled with a Cobra 150A ESC (Danlions Electric Industrial Co., Ltd.) using a standard 8 kHz PWM switching frequency. This programmable ESC has a maximum continuous current rating of 150 A and a burst current rating of 188 A for 15 s. Its operation voltage range is 7.4 V to 22.5 V (2 to 6 cells). This ESC was selected because its current limit is well above that of the motor, which adds a security layer to the testbed and helps prevent any failure in the event of a current jump. The motor is controlled using a typical PWM signal from 1000 µs to 2000 µs.

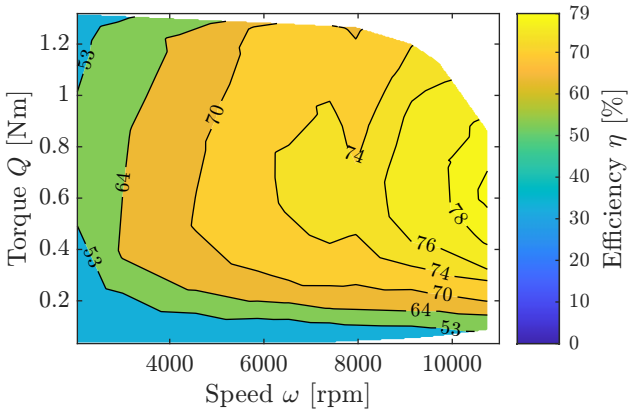

(a) Motor 4130/12 KV540 with Cobra 150A ESC

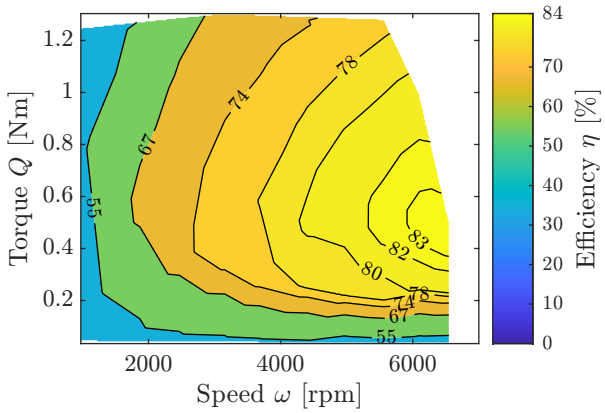

(b) Motor 4130/20 KV300 with Cobra 150A ESC

Figure 5. Efficiency maps of characterized motors

TABLE II: Characterized motors technical specifications

Specification	**Cobra 4130/12**	**Cobra 4130/20**
Number of Stator Slots	12	12
Number of Magnet Poles	14	14
Motor Wind	12 Turn Delta	20 Turn Delta
Motor Kv Value	540 rpm/V	300 rpm/V
Resistance per Phase	0.029 Ω	0.069 Ω
Resistance Phase to Phase	0.019 Ω	0.046 Ω
Maximum Continuous Current	65 A	52 A
PWM Frequency	8 kHz	8 kHz

Fig. 5 illustrates the efficiency of the two motors tested in this study. Efficiency maps are essential for evaluating the motor's performance throughout its entire torque-speed spectrum, offering valuable insights into operational characteristics. In particular, in mobile applications, it is advantageous to operate the motor within high-efficiency zones to maximize battery life. According to Fig. 5a and 5b, the high-efficiency zone is concentrated in the higher speeds region with midrange torque. In fact, the maximum efficiency of both motors can be found right at the limit of full power and full speed, which is common for BLDC motors. The Cobra 4130/12 motor shows a peak efficiency of 79 % at full throttle and 0.65 N m of torque. The Cobra 4130/20 motor, on the other hand, has a maximum efficiency of 83 % also at full speed, but 0.45 N m.

Furthermore, comparing Fig. 5a and 5b shows the importance of selecting the right component for a mission. Although similar in size, the Cobra 4130/20 performs at much higher efficiency than the Cobra 4130/12 for almost any given speed/torque situation, while the 4130/12 can operate at almost twice the speed of the 4130/20.

In order to assess the effect of the ESC on efficiency, the Cobra 4130/12 was characterized again with another ESC. The FLAME 80A (T-MOTOR) has a current limit of 80 A and a maximum current of 120 A for 10 s. It has an operating voltage range of 22.2 V to 44.4 V (6 to 12 cells). As can be seen in Fig. 6, the change of component seems to have a positive effect as the overall efficiency and the maximal value climbed to 82 %. The best efficiency still occurs at the maximum speed, but the optimal torque decreases slightly to about 0.55 N m. Although it had a positive effect on performance, the cause cannot be clearly identified. More testing is needed to clearly define the characteristics that affect the efficiency of the ESC.

The generated efficiency maps appear to contain some noise as the level lines are not always smooth. This phenomenon could have various origins. Even if the belt greatly reduced the vibration from the two-motor spinning, some level of vibration can still be observed or heard during the tests. The choice of $n = 10$ discretizations may not produce enough data points to generate a smooth curve, and additional roughness can come from the interpolation process.

IV. Conclusion

This study provided a low-cost characterization method to quickly assess the efficiency of a BLDC motor and ESC combo for all of its torque-speed range. For this purpose, a belt-driven dynamometer was designed. The belt configuration proved to be a low-cost solution to rotordynamic challenges while providing adaptability for various motor sizes. Using a generator as a resistance made it possible to redirect the

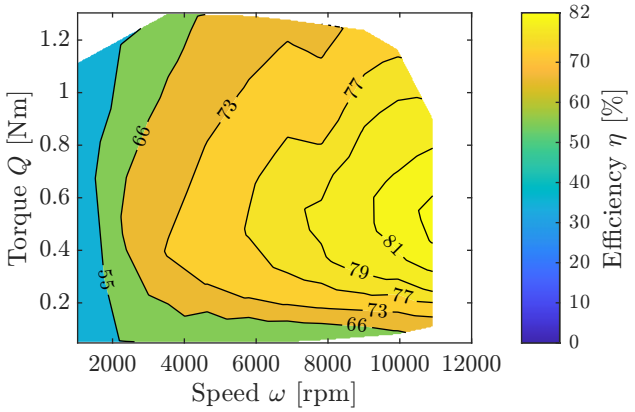

Figure 6. Efficiency map for motor 4130/12 KV540 with FLAME 80A

excess power in the DC bus and reduce the load on the power supply. The dynamometer, paired with Tyto Robotic's Flight Stand 15, allows for a simple and quick characterization of drone-sized BLDC motors. The testbed has since been used to characterize two motors with their ESC under real-world conditions. The motors were powered by LiPo batteries, controlled via standard ESC, and with active cooling just as they would be in flight.

It was shown that changing the ESC can have an impact on performance. However, the root cause of the variation in efficiency has not yet been determined. The next step in assessing the effect the ESC has on efficiency will be to test while modifying the built-in parameters available in some advanced drives.

As mentioned earlier, all characterizations were performed with four batteries in parallel in an effort to supply constant power throughout the process. It is known that the supplied voltage also has an effect on efficiency [9]. Further testing with actual power supplies that can deliver a true constant voltage could provide insight into how battery drainage in flight affects the efficiency of the powertrain.

Knowing the efficiency of the motor and its ESC, although game-changing, is not enough to precisely predict the overall performance of a drone. In order to make informed predictions, one must also know the efficiency of the propeller. The next step would be wind tunnel characterization of off-the-shelf propellers to get a complete picture of powertrain efficiency. The pairing of the two maps would allow the powertrain designer to optimize the performance for the mission specification, especially for airplane powertrains that can see a much wider variability in operating conditions than slow-flying multicopters.

The method discussed here is oriented for drone applications but has a much larger pool of applications. This low-cost method could be used for academic purposes to teach students to choose and use these components better and to understand the impact of the combination of some of them. Access to a drone-sized BLDC efficiency map opens the door to better powertrain design and extended flight time.

V. Acknowledgements

The author thanks Mr. Charles Blouin and Mr. Baiyun Tang of Tyto Robotics for their support and input, as well as for providing the equipment that made this study possible. This project was funded through a grant provided by CRIAQ (DEEPS).

References

[1] USI, "How Drones Have Changed The World." [Online]. Available: https://www.flyusi.org/blog/how-drones-have-changed-the-world

[2] D. L. Gabriel, J. Meyer, and F. Du Plessis, "Brushless DC motor characterisation and selection for a fixed wing UAV," in *IEEE Africon '11*. Victoria Falls, Livingstone, Zambia: IEEE, Sep. 2011, pp. 1–6. [Online]. Available: http://ieeexplore.ieee.org/document/6072087/

[3] T.-H. Hsieh, S. H. Yeon, and H. Herr, "Energy Efficiency and Performance Evaluation of an Exterior-Rotor Brushless DC Motor and Drive System across the Full Operating Range," *Actuators*, vol. 12, no. 8, p. 318, Aug. 2023. [Online]. Available: https://www.mdpi.com/2076-0825/12/8/318

[4] E. Agamloh and A. Nagorny, "An overview of efficiency and loss characterization of fractional horsepower motors," *IEEE Transactions on Industrial Electronics*, pp. 1–1, 2012. [Online]. Available: http://ieeexplore.ieee.org/document/6202686/

[5] U. H. Lee, C.-W. Pan, and E. J. Rouse, "Empirical Characterization of a High-performance Exterior-rotor Type Brushless DC Motor and Drive," in *2019 IEEE/RSJ International Conference on Intelligent Robots and Systems (IROS)*. Macau, China: IEEE, Nov. 2019, pp. 8018–8025. [Online]. Available: https://ieeexplore.ieee.org/document/8967626/

[6] C. R. Green and R. A. McDonald, "Modeling and Test of the Efficiency of Electronic Speed Controllers for Brushless DC Motors," in *15th AIAA Aviation Technology, Integration, and Operations Conference*, ser. AIAA AVIATION Forum. American Institute of Aeronautics and Astronautics, Jun. 2015. [Online]. Available: https://arc.aiaa.org/doi/10.2514/6.2015-3191

[7] Y.-C. Tian, M. O. Tadé, and J. Tang, "A nonlinear PID controller with applications," *IFAC Proceedings Volumes*, vol. 32, no. 2, pp. 2657–2661, Jul. 1999. [Online]. Available: https://linkinghub.elsevier.com/retrieve/pii/S1474667017564526

[8] G. Zaidner, S. Korotkin, E. Shteimberg, A. Ellenbogen, M. Arad, and Y. Cohen, "Non linear PID and its application in process control," in *2010 IEEE 26-Th Convention of Electrical and Electronics Engineers in Israel*. Eilat, Israel: IEEE, Nov. 2010, pp. 000 574–000 577. [Online]. Available: http://ieeexplore.ieee.org/document/5662155/

[9] J. M. Tabora, L. Correa Dos Santos Júnior, E. Ortiz De Matos, T. Mota Soares, A. R. Arrifano Manito, M. E. De Lima Tostes, and U. Holanda Bezerra, "Exploring the Effects of Voltage Variation and Load on the Electrical and Thermal Performance of Permanent-Magnet Synchronous Motors," *Energies*, vol. 17, no. 1, p. 8, Dec. 2023. [Online]. Available: https://www.mdpi.com/1996-1073/17/1/8